crystals

MDPI

Article

Sonoelectrochemical Nanoarchitectonics of Crystalline Mesoporous Magnetite @ Manganese Oxide Nanocomposite as an Alternate Anode Material for Energy-Storage Applications

Jayaraman Kalidass [1], Sambandam Anandan [2] and Thirugnanasambandam Sivasankar [1,*]

[1] Department of Chemical Engineering, National Institute of Technology Tiruchirappalli, Tamil Nadu 620015, India
[2] Department of Chemistry, National Institute of Technology Tiruchirappalli, Tamil Nadu 620015, India
* Correspondence: sivasankar9@gmail.com or ssankar@nitt.edu; Tel.: +91-431-2503121

Abstract: In this report, the synergetic sonoelectrochemical method was utilized to produce magnetite nanoparticles was doped with MnO_2 with the assistance of ultrasound to form nanoarchitectonic magnetic crystals with a mesoporous magnetite @ manganese dioxide (m-Fe_3O_4@MnO_2) hybrid nanostructure. The hybrid nanocomposite was rapidly produced based on the nucleation and growth of pure iron-oxide nanocrystals in the electrochemical system. The nanocomposite was pure, highly amorphous, and mesoporous in nature; the magnetite was spherical in shape, with an average diameter of 45 ± 10 nm and a MnO_2-plane length of 420 ± 30 nm. The stability of the pure m-Fe_3O_4 was enhanced from 89.61 to 94.04% with negligible weight loss after adding manganese dioxide and the stable formation of the hybrid nanostructure. Based on the superior results of the material, it was utilized as an anode material in Li-ion batteries. The m-Fe_3O_4@MnO_2 hybrid nanostructure had a highly active surface area, which enhanced the interfacial interaction between the Li-ion and the metal surface; it delivered 1513 mAh g^{-1} and 1290 mAh g^{-1} as the first specific discharge and charge capacity, respectively, with 85% coulombic efficiency, and it showed an excellent cyclic reversibility of 660 mAh g^{-1} with a coulombic efficiency of almost 99% at current density of 1.0 A g^{-1}.

Keywords: Fe_3O_4@MnO_2 nanocomposite; sonoelectrochemistry; anode; Li-ion battery

Citation: Kalidass, J.; Anandan, S.; Sivasankar, T. Sonoelectrochemical Nanoarchitectonics of Crystalline Mesoporous Magnetite @ Manganese Oxide Nanocomposite as an Alternate Anode Material for Energy-Storage Applications. *Crystals* **2023**, *13*, 557. https://doi.org/10.3390/cryst13040557

Academic Editors: Faxing Wang and Dah-Shyang Tsai

Received: 27 February 2023
Revised: 21 March 2023
Accepted: 22 March 2023
Published: 23 March 2023

1. Introduction

The emerging development of advanced transport systems and portable electronic devices drives the requirement for high-performing energy-conversion and -storage technology [1]. This technological breakthrough is essentially reliant on the evolution of electrochemical devices, such as fuel cells, batteries, supercapacitors, etc., in which Li-ion battery technology is becoming highly significant, since it has many valuable features, including high efficiency, high energy density, long cycle life, etc. [2]. Currently, researchers are focusing on the design of functionalized nanomaterials for enhancing energy efficiency and improving thermal performance in order to attain an optimized design enclosure [3–5]. However, the challenges facing the commercial application of the graphitic anodes, including their terminal resistance, capacity limitations, and low-temperature operations, need to be overcome by replacing electroactive metals and their various derivatives [6]. Recent studies suggested that transition-metal oxide materials could surmount these challenges, since they have a high theoretical specific capacity range (~500 to 1000 mAh g^{-1}) and excellent cycle performance. Iron-based materials are becoming promising anode materials among various transition-metal oxides because of their large availability, eco-friendliness, and inexpensive nature [7]. Since mesoporous magnetite (m-Fe_3O_4) nanoparticles in particular demonstrate the recommended magnetic properties and dynamic activities, it is largely utilized in other potential applications, such as drug delivery [8], pollutant removal [9], wastewater treatment [10], heavy metal removal [11] etc.

The current approaches to the synthesis of m-Fe_3O_4 nanoparticles, such as solvothermal and thermal decomposition methods, are more time-consuming and highly temperature-dependent [12]. To overcome these limitations with feasible synthesis conditions, a simple chimie douce (soft chemical) approach is utilized for the one-pot synthesis of high-quality magnetite nanoparticles in a very short time with the coupling of an electrochemical setup and ultrasound. Here, in this sonoelectrochemical system, the rapid formation of magnetite occurs, followed by the combined influence of ultrasound cavitation and electrochemical oxidation-reduction reactions [13]. The redox reactions between the electrodes and the electrolyte help to release and accept valance electrons from the metallic surface, which leads to the nucleation and growth of nanocrystals over the surface of the electrode. When the microbubble collapses, through the uncertain conditions, including the extreme temperature (~5000 K), ultra-fast cooling rate (~10^{10} Ks^{-1}), and high pressure (~20 MPa), countless radicals are created. At the same time, the formation of small vapor-filled microbubbles through the cavitation phenomenon enhances the mass transport inside the electrolyte system through highly active radicals from the rapid collapse, which helps to detach the deposition of the iron oxide from the conducting electrode's surface. Eventually, pure crystalline magnetic nanoparticles settle as sediment [14]. Beyond achieving rapid synthesis through this method, the possibility of tuning the morphology in terms of shape and size patterns, long endurance, uniform dispersion, etc., could lead to the achievement of the desirable properties and yield a product with maximum conversion efficiency [15].

Since the synthesis of high-quality magnetite nanoparticles, the utilization of pure m-Fe_3O_4 nanomaterial as an anode material for Li-ion batteries has been followed by several modifications due to its volume-expansion nature during charge–discharge, its intrinsically poor conductivity, and the blocking of voids by lithium ions [16]. These limitations cause stress on the surface, which might lead to material deterioration, insufficient electron transfer, and the suppression of the diffusion mechanism. Hence, the electrochemical performance of the material becomes poor [17]. Therefore, it is important to tune the core structure with an effective material to mitigate the issue by stabilizing the m-Fe_3O_4. To this end, manganese oxide was chosen from among other transition-metal oxides because of its identical atomic properties and higher oxidation state, of up to seven. Furthermore, it is very compatible with iron oxides, with a similar crystal symmetry. In addition, its ease of preparation and high stability are important features in the selection and formation of a nanoarchitectonic hybrid nanostructure [18]. The electrochemical features and surface characterization of MnO_2 through the influence of various additives as a cathode for aqueous battery systems were investigated by Minakshi et al. [19–24]. However, the fabrication of metal-oxide electrodes with defined morphologies and structures to buffer the volume expansion during the charging–discharging cycles, and also to meet the demand for good lifetime performance still needs to be improved.

In this report, highly crystalline mesoporous magnetite (m-Fe_3O_4) nanoparticles were synthesized via a simple one-pot sonoelectrochemical method in a very short time. The m-Fe_3O_4 was successfully anchored with MnO_2 planes via ultrasound-induced self-organization, in which the nano-sized mesoporous Fe_3O_4 was uniformly dispersed or anchored in a desired pattern over the MnO_2 planes to form the m-Fe_3O_4@MnO_2 nanoarchitectonic hybrid nanostructure. This structure was then utilized as an anode material for a laboratory-fabricated lithium coin cell (CR2032). The electrochemical performance of the magnetite nanoparticles and magnetite-doped MnO_2 were studied. The effect of the doping of the MnO_2 with the m-Fe_3O_4 on the structural rearrangements, enhancements in surface area, and stability were analyzed. The nanoarchitectonic hybrid structure was studied for its thermal stability and surface area, which might influence electrochemical performance at high current densities.

2. Materials and Methods

Pure iron plates with 99.87% purity (0.5 milli meter thick) were procured from Tiruchirappalli industrial area, India. Electrolyte-salt sodium sulfate (Na_2SO_4), stabilizer thiourea

(CH_4N_2S), additive potassium chloride (KCl), and precursor potassium permanganate ($KMnO_4$) were obtained from Merck, India. Chemicals of high-purity grade were purchased and used without additional purification procedures. Water obtained after two distillations was used with 18.2 MΩ of resistance to prepare the required solutions for the synthesis of m-Fe_3O_4@MnO_2 nanoarchitectonic hybrid nanostructure.

2.1. Sonoelectrochemical Nanoarchitectonic Synthesis of m-Fe_3O_4@MnO_2 Hybrid Nanostructure

The nanoarchitectonic m-Fe_3O_4@MnO_2 hybrid nanostructure was created in a two-step ultrasonic processes. In the first step, magnetite nanoparticles were synthesized by employing sonoelectrochemical technique, as previously reported, under optimized conditions [25], in which the electrolyte volume was taken as 200 mL, which contained 0.25 M Na_2SO_4, 0.04 M thiourea, and 0.014 M KCl, and was maintained at 60 °C. The pure iron plates with known surface areas (1 cm^2 and 4 cm^2) were taken as working electrode (WE) and counter electrode (CE), respectively. They were preactivated by following ASTM standards to eliminate the unwanted oxide layer. Next, the surface preactivated electrodes were dried, insulated, and mounted at a distance of 1 cm inside the electrochemical cell. The combined driving force of constant current density (0.8 A cm^{-2}) and ultrasonic irradiation (60% amplitude) were introduced from galvanostat (PGSTAT302N, Metrohm Autolab, Netherland) and ultrasonic processor (Elma Transonic Digital T490DH, Gottlieb-Daimler-Straße 17, 78224 Singen (Hohentwiel), Germany, Emission frequency = 40 kHz). The schematic representation of experimental setup is shown in Figure 1. Once the system was sonoelectrochemically activated, the combined effect of redox reaction and cavitation phenomenon helped the rapid formation of magnetite nanoparticles as precipitates, which was verified by black color of solution. The product was magnetically collected and washed multiple times with water and ethanol.

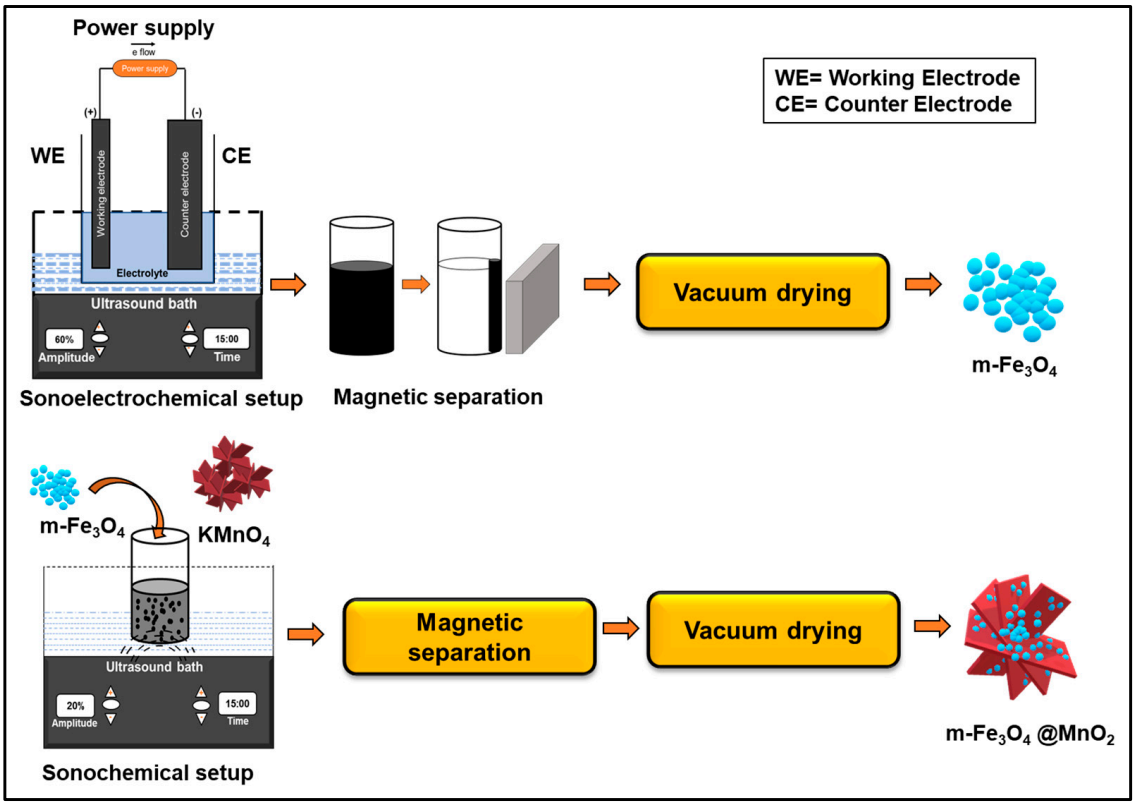

Figure 1. Schematic representation of experimental setup for m-Fe_3O_4@MnO_2 nanoarchitectonics.

In the second step, the nanoarchitectonic structures of m-Fe_3O_4@MnO_2 were synthesized via ultrasound method with a slight modification of previously reported work [26]:

m-Fe_3O_4 nanoparticles were dispersed in an aqueous solution of 0.03 M $KMnO_4$ and subjected to less-amplitude sonication for 15 min, in which the ultrasound induced self-arrangement of mesoporous Fe_3O_4 nanoparticles over an intended configuration of MnO_2 nano planes, forming a nanoarchitectonic hybrid nanostructure. The final product was magnetically collected, and dried at 45 °C in vacuum condition overnight.

2.2. Material Characterizations

The elemental composition-based purity analyses of working and counter electrodes carried out by X-ray fluorescence (XRF) (Olympus, Center Valley, PA, USA). Crystallographic plane positions of the prepared m-Fe_3O_4@MnO_2 hybrid nanostructure were identified in a range between 10° and 80° 2θ by X-ray Diffractometer (XRD) (Rigaku-Ultima-IV, Akishima-shi, Tokyo 196-8666, Japan), with the help of monochromatic CuKα_1 radiation. The presence of functional groups over the surface of the nanocomposite was noted at wavenumbers between 4000 and 400 cm^{-1} through Fourier Transform-Infrared Spectroscopy (FTIR) (Perkin Elmer, Waltham, MA, USA). The morphology studies with respect to shape and size patterns were conducted using electron-microscopic techniques (field-emission scanning electron microscope (FESEM) (ZEISS, Sigma, 73447 Oberkochen, Germany) and high-resolution transmission-electron microscope (HR-TEM) (JEM 2100, Tokyo, Japan)). Pore size and specific surface area were determined from nitrogen-adsorption–desorption-isotherm studies, using Quantachrome Nova Station, performed at 77 K. The enhancement in thermal stability was observed between room temperature (~30 °C) and 700 °C through thermogravimetric analysis (TGA) (Perkin Elmer, USA) in nitrogen atmosphere at a scan rate of 10 °C min^{-1}.

2.3. Electrochemical Characterization

The electrochemical performance of the sonoelectrochemically synthesized m-Fe_3O_4@MnO_2 hybrid nanostructure was measured by utilizing it as an anode in a laboratory-fabricated coin cell (CR2032), with Li metal chip acting as counter and reference electrode. The working electrode was formulated by mixing active material (m-Fe_3O_4@MnO_2), binder (PVDF), and conducting agent (Acetylene black) in 80:10:10 wt% with an appropriate volume of solvent, NMP (N-methyl-2-Pyrrolidone). The mass loading of the prepared slurry on 16-μm-thick copper foil was kept between 1.2 and 1.5 mg cm^{-2}. Lithium cells were assembled as a coin cell (CR2032) inside argon-filled vacuum glove box, in which the humidity and moisture were controlled at <10 ppm. The Celgard 2325 and $LiPF_6$ (EC:DMC:DEC = 1:1:1) were used as separator and electrolyte, respectively. The assembled cells were submitted to voltammetric studies in a potential window between 0.01 and 3.0 V at a scan rate of 0.1 mV s^{-1} via electrochemical workstation (PGSTAT302N, Metrohm Autolab, The Netherland). The galvanostatic charge–discharge was tested with a universal-battery-testing system (BTS4000-NEWARE).

3. Results and Discussion

3.1. Element-Based Purity Test

The element-based purity test on the iron-metal plates was carried out with a compact X-ray fluorescence spectroscopy. It was confirmed that the purity of the iron in the procured samples was 99.87%, with a very low manganese percentage. Therefore, it might be possible to utilize the metal plate as a working and counter electrode, which could be able to produce high-quality Fe_3O_4 nanoparticles in pure form through the sonoelectrochemical method.

3.2. Presence of Elements in the Nanocomposite

The presence of manganese oxide and magnetite through atomic vibrational stretching was confirmed by the FTIR spectrum, as shown in Figure 2. The decisive peak at 551 cm^{-1} depicts the Fe-O vibrational stretching of the magnetite nanoparticles, which moved slightly, to 609 cm^{-1}, as the transmittance value increased in the case of the sonoelectrochemical m-Fe_3O_4@MnO_2 hybrid nanostructure, where remarkable peaks at 566 and 545 cm^{-1}

were observed for the strong Mn-O stretching vibrations. This reduction and remarkable shift in the absorption value with respect to the wavenumber in the Fe-O stretching may have been due to the successful coordination of the Fe_3O_4 nanoparticles with the highly active manganese–oxygen group. This confirmed the presence of manganese oxide and magnetite together in the sonoelectrochemically prepared nanocomposite. The additional peaks around ~3400 cm^{-1} were ascribed to hydroxyl groups and ~1129, ~1645 cm^{-1} wavenumbers correspond to the carbon–oxygen stretching vibrations.

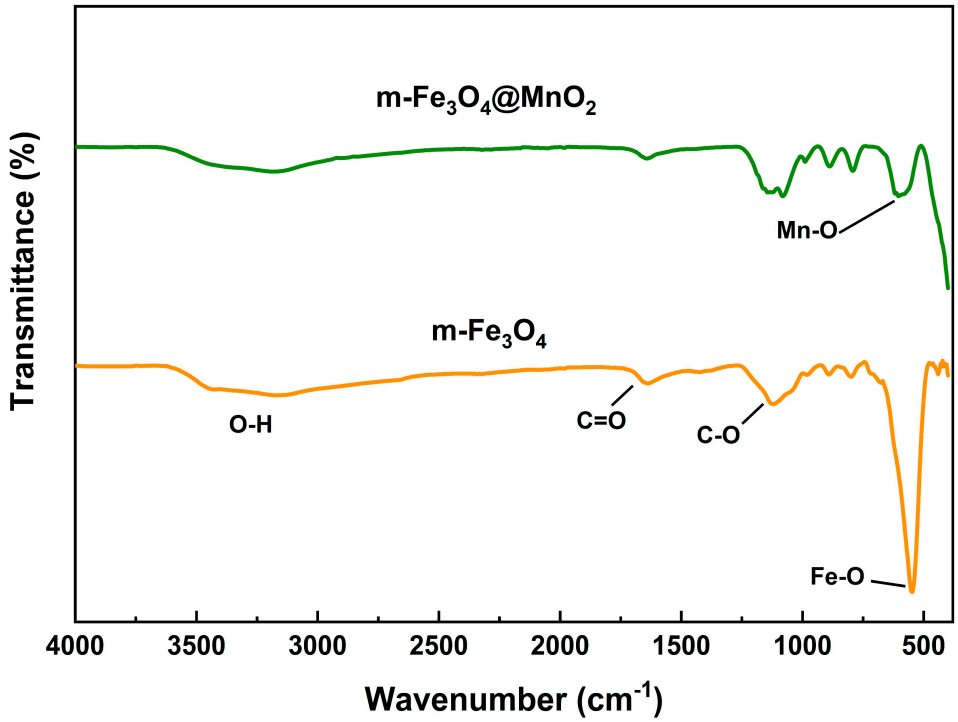

Figure 2. FTIR spectrum of m-Fe_3O_4 and m-Fe_3O_4@MnO_2 nanocomposites.

3.3. Material Characteristics of m-Fe_3O_4 and m-Fe_3O_4@MnO_2

The crystallographic studies of the samples were compared through X-ray diffractometric patterns, which are shown in Figure 3. It was observed that the samples were pure and amorphous in nature, with the predominant crystal planes (220), (311), (400), (422), (511), (440), and (533) located at 30.1°, 35.5°, 43.1°, 53.4°, 57°, 62.4°, and 74.2°, respectively, as shown in Figure 3A, corresponding to the inverse cubic spinel structure of Fe_3O_4 nanoparticles (JCPDS no. 00-19-0629). The average crystallite size was theoretically calculated from Scherrer's formula and found to be 41.42 nm. This result was clearly in line with the FESEM results, which are shown in Figure 4. In the case of the m-Fe_3O_4@MnO_2 hybrid nanostructure, the XRD patterns revealed many similar patterns, but with lower-intensity reflections (Figure 3B). This may have resulted from the lower concentration of the manganese precursor. However, with the slight shift, the less-intense peaks obtained at 12.3°, 21.1°, 30.1°, 36.6°, 57.1°, and 58.9°, ascribed to the (110), (200), (310), (211), (600), and (521) planes of manganese oxide, respectively, shown on the inset graph, represent the stoichiometric alteration between iron and manganese oxides (JCPDS no. 00-44-0141). The nonappearance of miscellaneous peaks reveals the purity and successful formation of the hybrid nanostructure.

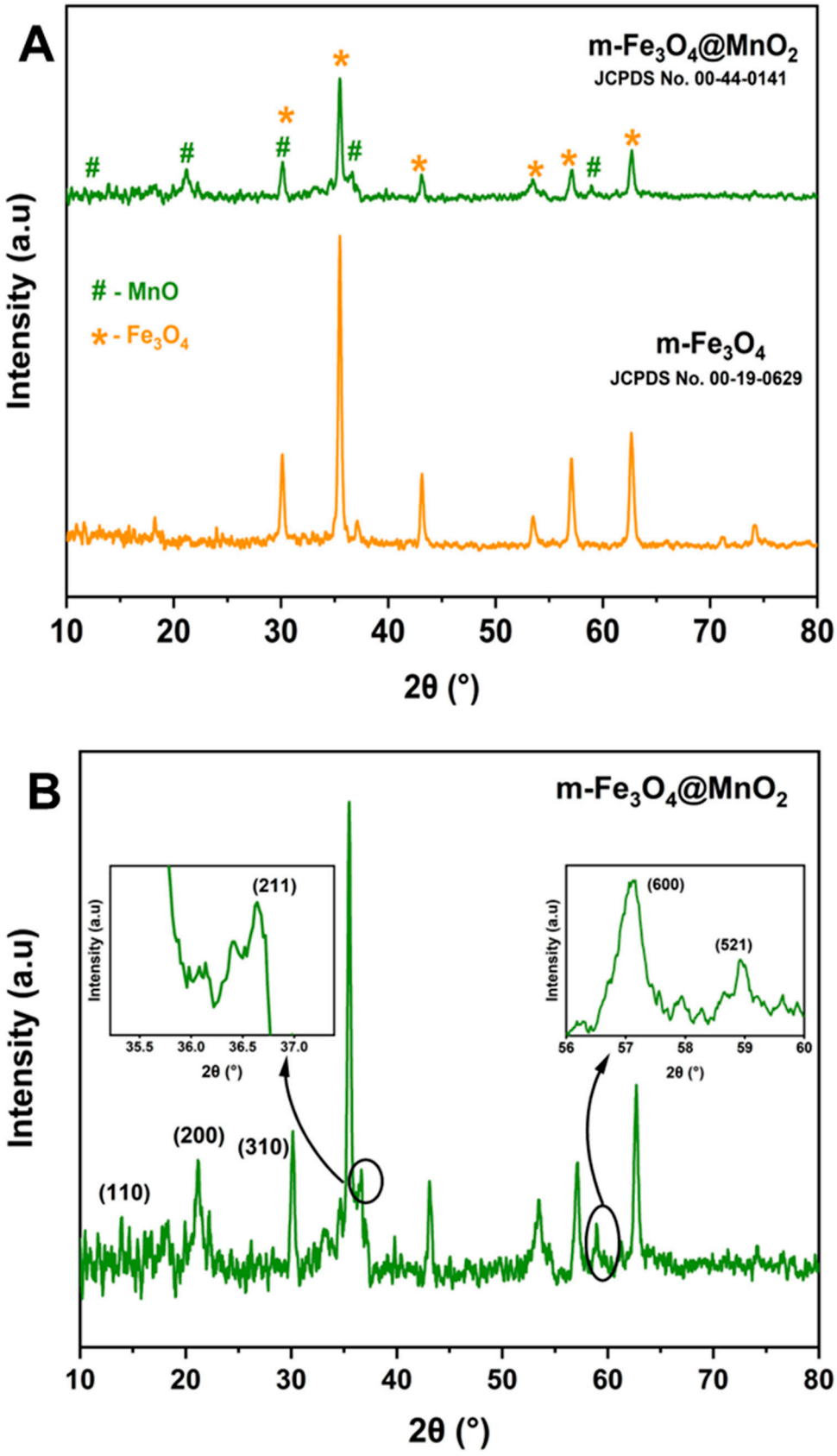

Figure 3. (**A**) Combined XRD patterns of m-Fe_3O_4 and m-Fe_3O_4@MnO_2 nanocomposite and (**B**) crystal planes of MnO_2 in the nanocomposite (JCPDS-00-44-0141).

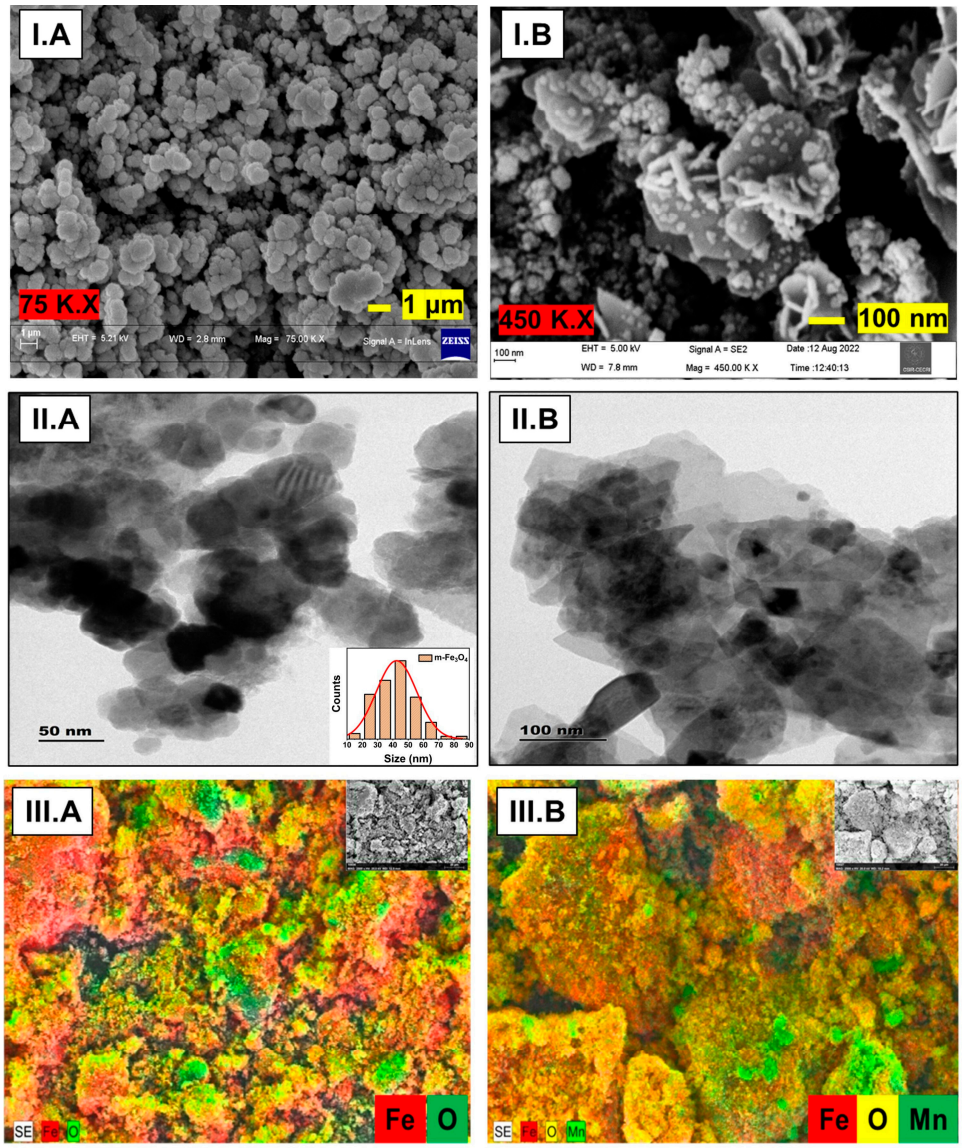

Figure 4. FESEM (**I**), HRTEM (**II**), and elemental mapping (**III**) of (**A**) m-Fe_3O_4 and (**B**) m-Fe_3O_4@MnO_2 nanocomposites.

The morphological studies to determine the shape and size characteristics of the nanocomposite through FESEM, HR-TEM analysis, and elemental mapping analysis were performed and the results are shown in Figure 4. The FESEM and HRTEM results showed that the sonoelectrochemically prepared m-Fe_3O_4 nanoparticles (Figure 4A) were spherical in shape, with a mean diameter of 45 $\pm$ 10 nm. The mean size of the magnetite was in good agreement with the crystallite size theoretically calculated from the XRD results. The synergetic effect of the cavitation processes led to the sudden increase in high temperatures after the bubble collapse, which, consequently, produced shock waves under extreme pressure conditions. All these mechanisms together accelerated the spherical formation of Fe_3O_4 nanoparticles. Further, the ultrasound induced the self-organization of the m-Fe_3O_4 over the surfaces of the MnO_2 planes with an average length of 420 $\pm$ 30 nm to form a nanoarchitectonic configuration (Figure 4B). The iron and oxygen elements in the mixture of the pure m-Fe_3O_4 were identified through the colors red and green, respectively, and, in the case of the m-Fe_3O_4@MnO_2 nanocomposite, the colors red, yellow and green were used to identify the presence of iron, oxygen, and manganese, respectively. It is believed that the anchoring effect of iron oxide nanoparticles on the MnO_2 planes can obviate the agglomeration nature of Fe_3O_4 nanoparticles during charge–discharge studies.

The porous nature of the prepared samples was determined through nitrogen-adsorption–desorption studies under isothermal conditions (77 K) after degassing at 110 °C for 12 h. The inferences of the surface area and pore characteristics are shown in Figure 5. Based on the results, the m-Fe_3O_4 nanoparticles and the m-Fe_3O_4@MnO_2 hybrid nanostructure possessed type IV isotherms and loops with a H3 hysteresis structure. This confirms that both samples were of a mesoporous nature. The individual contributions of the planes and spherical nanoparticles during the isotherm kinetics caused the enhancement of the surface area from 121.876 to 385.704 m^2 g^{-1}. This was mainly because of the nucleation of the nanocrystallites after the induction caused by the ultrasound resulting in the rapid 'Ostwald ripening' process which formed highly ordered manganese planes with active sites. As a summary of the BJH desorption, the pore volume and pore diameter of the m-Fe_3O_4@MnO_2 hybrid nanostructure were measured as 0.587 cm^3 g^{-1} and 2.098 nm, respectively.

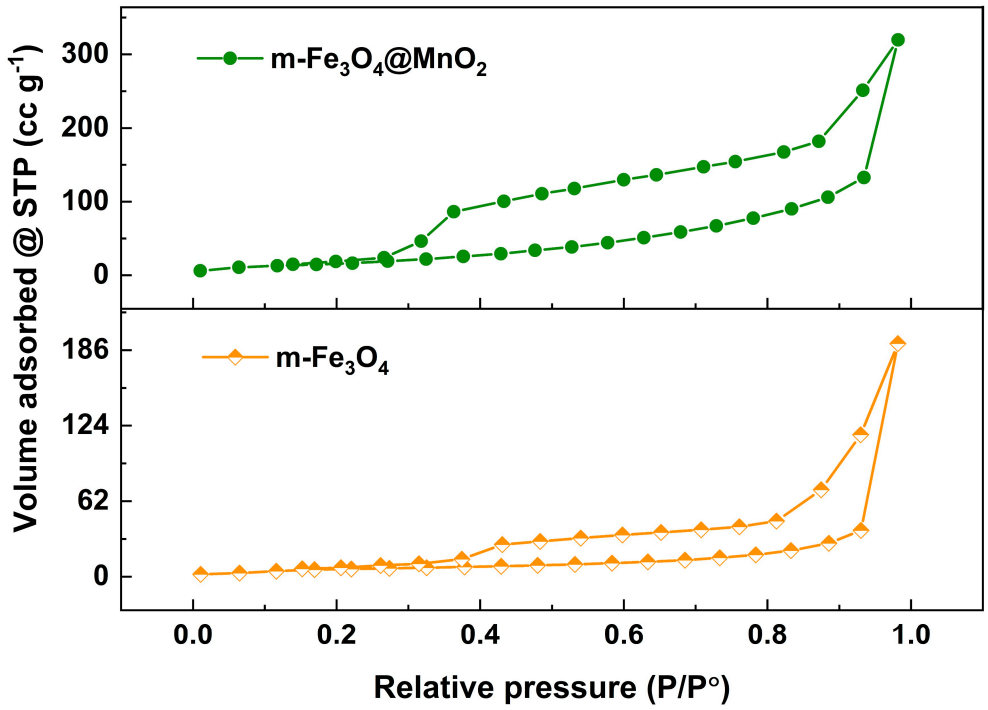

Figure 5. BET results of m-Fe_3O_4 and m-Fe_3O_4@MnO_2 nanocomposites.

The thermal stability of the m-Fe_3O_4 and Fe_3O_4@MnO_2 hybrid nanostructures were and the results are shown in Figure 6. The overall weight loss of the m-Fe_3O_4 was found to be 10.4%, while the preliminary weight loss (3.57%) from room temperature to 150 °C was identified as the elimination of the oxygen–hydrogen (-OH) linked functional groups, which might have been adsorbed on the surface of the material in connection with aqueous solution and residue from the ethanol washing. The removal of organosulfur from the electrolytes occurred between 150 °C and 300 °C, and weight loss of 5.15% was observed. The additional removal of weight from 300 °C to 700 °C (1.58%) might have cleared the halide off the KCl salt. Finally, the physical transition of the magnetite to hematite occurred after 700 °C. With the addition of the manganese salt, the thermal stability of the Fe_3O_4 was enhanced from 89.61 to 94.04%, with almost negligible weight loss, which might have been due to the formation of a hybrid nanostructure resulting from the effective cavitation induced by the ultrasound radiation. Because of the nanosized nature and narrow distribution of the m-Fe_3O_4, it easily reacted with the surfaces of the MnO_2 planes, which acted as a thermal resistive layer. Additionally, this layer stabilized the physical transition of the magnetite against further losses.

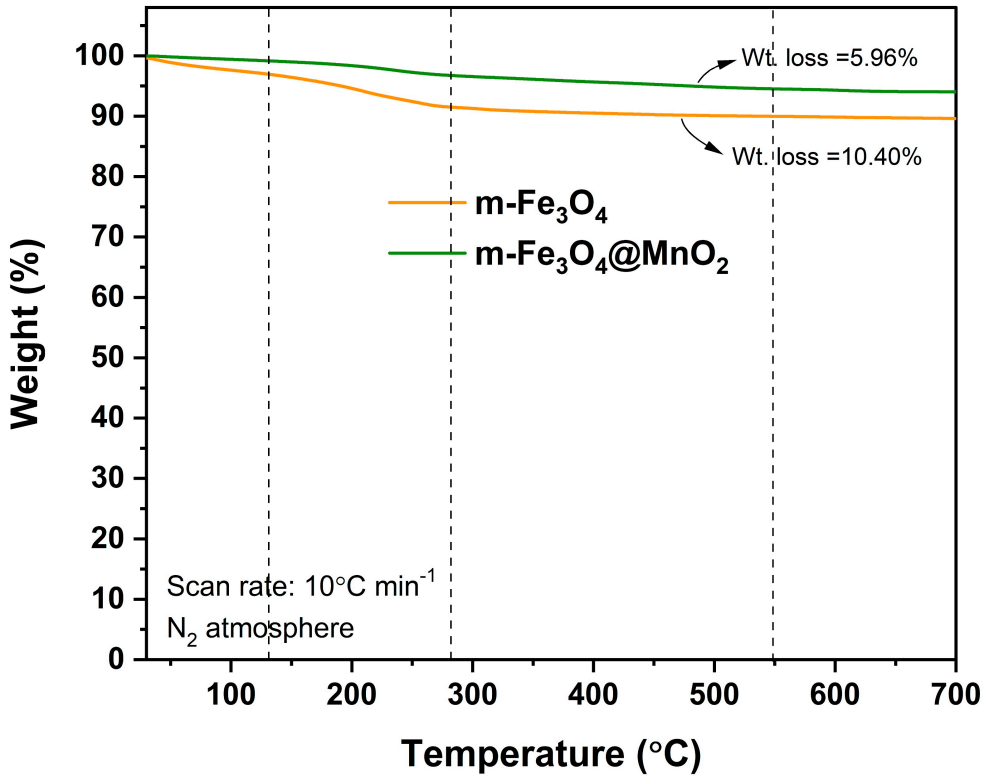

Figure 6. TGA results of m-Fe_3O_4 and m-Fe_3O_4@MnO_2 nanocomposite.

3.4. Electrochemical Performance of m-Fe_3O_4 and m-Fe_3O_4@MnO_2

Figure 7 (left) shows the cyclic voltametric results of the m-Fe_3O_4 and m-Fe_3O_4@MnO_2 electrodes for three scans carried out at a scan rate of 0.1 mV s^{-1}. Major reduction peaks were observed for both samples at around ~1 V, and the oxidation peaks were near ~0.5 V for the m-Fe_3O_4 and 1.67 V for the m-Fe_3O_4@MnO_2 electrodes, with respect to the standard lithium reduction potential. The discharge process for the first scan revealed the reduction peak for the m-Fe_3O_4 electrode at 0.965 V, which shifted and started to overlap at 0.96 V in the two subsequent scans. For the m-Fe_3O_4@MnO_2, the reduction peaks were obtained at 0.482 V for the first cycle, and the shift and overlap occurred at 0.46 V. During the discharge process, the shifting and overlapping of the voltametric curves occurred due to the formation of the solid-electrolyte interface layer (SEI) after the Li-ions were inserted into the mesoporous metal oxide and through the formation of Li_2O dendrites. At the same time, the reduction of the trivalent metal ions (Fe (III) and Mn(III)) into zero valent metal (Fe (0) and Mn (0)) occurred during the Li insertion. In the case of charging, the reversible process took place and vice versa; the oxidation peak was observed at 0.48 V for the m-Fe_3O_4, and further, it was smoothened in the case of the m-Fe_3O_4@MnO_2 electrode. This may have been due to the strong structural rearrangement between the active material and the electrolyte during the oxidation process. During the oxidation process, the active materials returned to their oxide form (Fe_3O_4 and MnO_2). These cyclic voltammograms were agreeable with the voltage plateau in the galvanostatic charge–discharge (GCD) studies.

The Li storage properties were identified for the sonoelectrochemically prepared nanocomposite through the laboratory-fabricated coin cells in a half-cell configuration, and the GCD studies were performed at a current density of 200 mA cm^{-2} in the range between 0.01 and 3.0 V (Figure 7 right). The voltage platform occurred at nearly 0.7 V with a sloping tendency for the m-Fe_3O_4 electrode, and it delivered 1278 mAh g^{-1} as a maximum first-discharge-specific capacity and 868 mAh g^{-1} as a charge-specific capacity with a coulombic efficiency of almost 68%. The m-Fe_3O_4@MnO_2 electrode delivered the first maximum discharge and charge capacities of 1513 mAh g^{-1} and 1290 mAh g^{-1}, with a coulombic efficiency of 85%. The increment in the first-discharge capacity might have been due to

the structural enhancement of the m-Fe_3O_4 with MnO_2, resulting in the enhancement of the material properties in terms of the increasing surface area and stability of the m-Fe_3O_4 nanoparticles, according to the BET and TGA results. The overlapping of the curves for the next two consecutive cycles with a coulombic efficiency of ~99% demonstrates the stable formation of the solid-electrolyte -interface (SEI) layer.

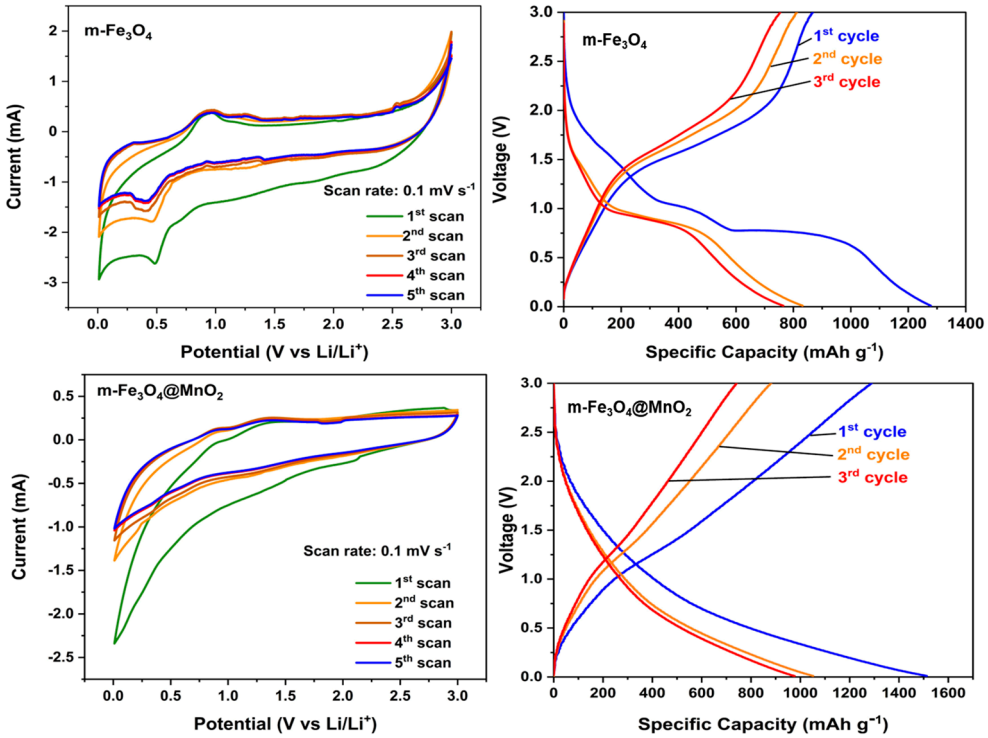

Figure 7. Cyclic voltammetry (**left**) and GCD (**right**) results of m-Fe_3O_4 and m-Fe_3O_4@MnO_2 nanocomposites.

Figure 8 shows the cyclability of the prepared nanocomposite; the charge-discharge cycles were performed at a current density of 1.0 A g^{-1} for 100 cycles. At the end of the100 cycles, the nanocomposite manifested a reversible capacity of 660 mAh g^{-1}, with a coulombic efficiency of almost 99%.

Table 1 shows the comparative data of various recent synthesis methods for the Fe_3O_4@MnO_2 nanocomposite with respect to various synthesis factors, such as the synthesis time, temperature, atmosphere, and material properties, for multiple applications. The comparative data clearly depict that the sonoelectrochemical synthesis method is an effective method to prepare high-purity m-Fe_3O_4@MnO_2 nanocomposites in less synthesis time, at low temperatures, and under open-atmosphere conditions. Table 2 and Figure 9 display the performance-comparison data of various different anode materials for various energy applications. The electrochemical comparison data of the sonoelectrochemically self-assembled nanocomposite were comparatively good, suggesting that this nanocomposite could be a better replacement anode for graphite electrodes in current Li-ion batteries.

Table 1. Comparative data of various synthesis methods for Fe_3O_4@MnO_2 nanocomposite with the current method.

Material	Method	Synthesis Time	Temp. (°C)	Atmosphere	Size		Surface Area (m^2 g^{-1})	Application	Reference
					Fe_3O_4 (nm)	MnO_2 (nm)			
PR-Fe@MnO_2	Carbonization	2 h	800 °C	N_2	-	-	1073	Supercapacitor	[27]
α-MnO_2/Fe_3O_4 nanocomposite	Hydrothermal	4 h	110 °C	Open	22 ± 5	50 ± 10 dia., ~1 μ length	-	Degradation	[28]
Fe_3O_4-MnO_2	Co-precipitation	2 h	70 °C	Open	-	-	127	Catalyst	[29]
Fe_3O_4-α-MnO_2 nanoflower	Hydrothermal	2 + 10 h	80 °C, 120 °C	Open	50–60	-	-	Catalyst	[30]
Core-shell nanoflowers Fe_3O_4@MnO_2	Solvothermal	8 + 6 h	200 °C, 120 °C	Open	-	-	-	Detector	[31]
m-Fe_3O_4@MnO_2 hybrid nanostructure	Sonoelectrochemical	15 + 15 min	60 °C	Open	45 ± 10	420 + 30	385.7	Anode	This paper

Table 2. Performance-comparison data of different recent anode materials for various energy applications.

Material	Structure	Synthesis Method	Synthesis Duration	Cd A g^{-1}	1st Cycle $C_{Discharge}$ mAh g^{-1}	C_{Charge} mAh g^{-1}	Cyclic Stability Cycles	Cd A g^{-1}	C_{Rev} mAh g^{-1}	Ref.
$MnFe_2O_4$/C	Hollow nanospheres	Hydrothermal, carbonization, self-etching	200 °C for 8 h 160 °C for 4 h RT for 15 h	0.2	1219	~980	60	0.2	973	[32]
$MnFe_2O_4$	Porous microrods	Microemulsion, annealing	RT for 9 h 500 °C for 2 h	-	1336	~937	1000	1	630	[33]
$MnFe_2O_4$/GN	NPs decorated on sheet	Hydrothermal	180 °C for 12 h	0.2	1369	838	200	1	768	[34]
$MnFe_2O_4$/rGO	NPs decorated on sheet	Co-precipitation	90 °C for 4 h	0.05	1256.5	794	200	1	581.2	[35]
Mn_2O_3/Fe_2O_3	Microspheres	Solvothermal and annealing	150 °C for 12 h, 800 °C for 5 h	1	1403	886	500	1	750	[36]
Fe_2O_3/MnO_2	Microspheres	Hydrothermal	600 °C for 3 h 80 °C for 4 h 600 °C for 3 h	0.1	1675.6	1051.3	500	0.5	494	[37]
Fe_3O_4@(C-MnO_2)	Cubic encapsulation	Hydrothermal, sintering, ultrasonication	180 °C for 6 h, 400 °C for 3 h, 600 °C for 4 h, 180 °C for 6 h	0.1	1786	~1200	150	0.1	979	[38]
$MnMoO_4$@C	Nanorods	Precipitation, calcination, hydrothermal	RT for 1 h, 500 °C for 3 h, 180 °C for 12 h	0.1C	1482	1021	200	0.1	1050	[39]
$NiMoO_4$	Nanordods	Solution combustion	300 °C for 3 h	0.05	665	365	100	0.05	245	[40]
$Fe_2Mo_3O_8$	Block-like structure	High-temperature solid-state reaction	1000 °C for 8 h under 8 MPa pressure	0.05	898.7	~870	800	0.5	240	[41]
$ZnMoO_4$/rGO	Irregular plate	Hydrothermal	160 °C for 8 h	0.1	2391.2	~850	100	0.1	632	[42]
m-Fe_3O_4/MnO_2	NPs decorated on sheet	Sonoelectrochemical	60 °C for 15 min RT for 15 min	0.2	1513	1290	100	1	660	This work

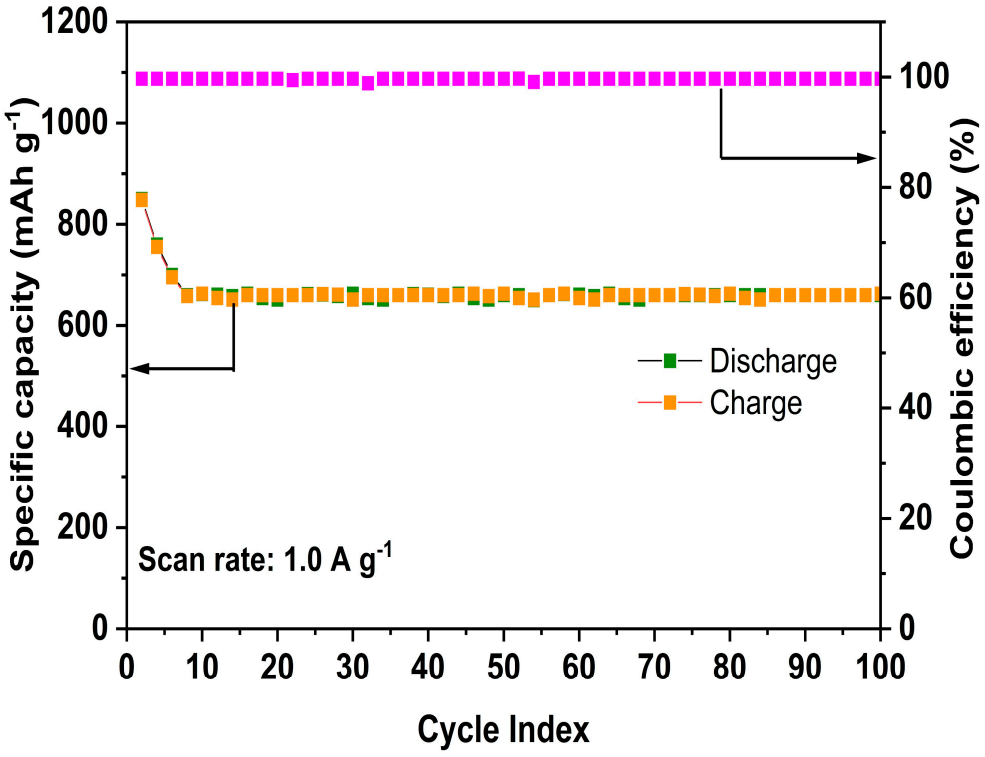

Figure 8. Cyclic performance of m-Fe_3O_4@MnO_2 nanocomposite at current density of 1.0 A g^{-1}.

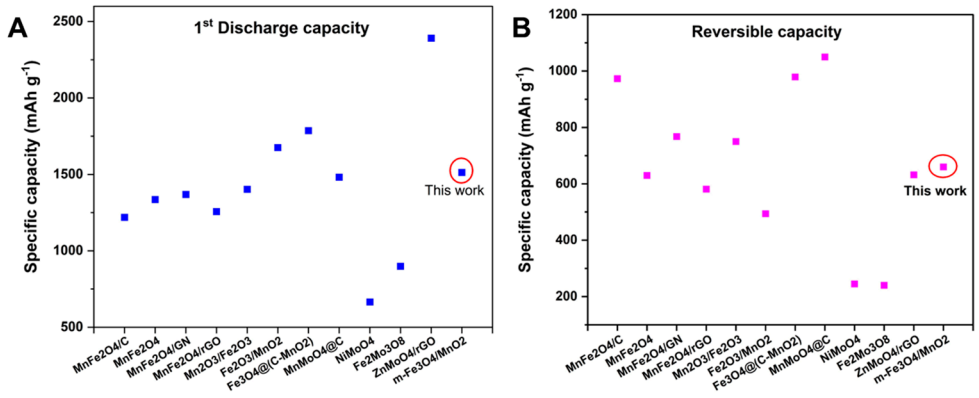

Figure 9. Electrochemical performance-comparison chart of manganese-based anodes.

4. Conclusions

In summary, the preparation of a highly crystalline mesoporous magnetite @ manganese oxide hybrid nanostructure was performed via the synergetic sonoelectrochemical approach over a very short synthesis time, and it was utilized as an anode material for a laboratory-fabricated Li-ion coin cell (CR2032). The results show that the prepared hybrid nanostructure not only improved the material quality in terms of stability and surface area, but also improved the electrochemical performance. Since the structural modifications obviated the volume expansion of m-Fe_3O_4, enhancement, which produced stable, reversible capacity, was observed. As a result, the m-Fe_3O_4@MnO_2 delivered a maximum specific discharge and charge capacity of 1513 mAh g^{-1} and 1290 mAh g^{-1}, respectively, with a coulombic efficiency of 85%. The cyclic-performance results, which were obtained at 1.0 A g^{-1} over 100 cycles, proved that the nanocomposite manifested a reversible capacity of 660 mAh g^{-1}, with a coulombic efficiency of almost 99%. Based on the delivery of stable and reversible capacity with greater electrochemical performance by the the sonoelectro-

chemically fabricated m-Fe_3O_4@MnO_2 hybrid nanostructure, it can be appropriately and favorably advanced as an anode material for future Li-ion-battery technology.

Author Contributions: Conceptualization, methodology, formal analysis, writing—original draft preparation, J.K.; resources, data curation, S.A.; validation, investigation, resources, data curation, review and editing, supervision, project administration, T.S. All authors have read and agreed to the published version of the manuscript.

Funding: This research received no external funding.

Data Availability Statement: Not applicable.

Acknowledgments: Jayaraman Kalidass acknowledges the Ministry of Education (MoE) for the Ph.D. scholarship.

Conflicts of Interest: The authors declare no conflict of interest.

References

1. Rahman, M.M.; Oni, A.O.; Gemechu, E.; Kumar, A. Assessment of Energy Storage Technologies: A Review. *Energy Convers. Manag.* **2020**, *223*, 113295. [CrossRef]
2. Kim, T.; Song, W.; Son, D.-Y.; Ono, L.K.; Qi, Y. Lithium-Ion Batteries: Outlook on Present, Future, and Hybridized Technologies. *J. Mater. Chem. A* **2019**, *7*, 2942–2964. [CrossRef]
3. Ghalkhani, M.; Habibi, S. Review of the Li-Ion Battery, Thermal Management, and AI-Based Battery Management System for EV Application. *Energies* **2023**, *16*, 185. [CrossRef]
4. Yoshino, A. The Lithium-Ion Battery: Two Breakthroughs in Development and Two Reasons for the Nobel Prize. *BCSJ* **2022**, *95*, 195–197. [CrossRef]
5. Ariga, K. Nanoarchitectonics: What's Coming next after Nanotechnology? *Nanoscale Horiz.* **2021**, *6*, 364–378. [CrossRef]
6. Zhang, H.; Yang, Y.; Ren, D.; Wang, L.; He, X. Graphite as Anode Materials: Fundamental Mechanism, Recent Progress and Advances. *Energy Storage Mater.* **2021**, *36*, 147–170. [CrossRef]
7. Qi, S.; Xu, B.; Tiong, V.T.; Hu, J.; Ma, J. Progress on Iron Oxides and Chalcogenides as Anodes for Sodium-Ion Batteries. *Chem. Eng. J.* **2020**, *379*, 122261. [CrossRef]
8. Yew, Y.P.; Shameli, K.; Miyake, M.; Ahmad Khairudin, N.B.B.; Mohamad, S.E.B.; Naiki, T.; Lee, K.X. Green Biosynthesis of Superparamagnetic Magnetite Fe_3O_4 Nanoparticles and Biomedical Applications in Targeted Anticancer Drug Delivery System: A Review. *Arab. J. Chem.* **2020**, *13*, 2287–2308. [CrossRef]
9. Tadesse, A.; RamaDevi, D.; Hagos, M.; Battu, G.; Basavaiah, K. Synthesis of Nitrogen Doped Carbon Quantum Dots/Magnetite Nanocomposites for Efficient Removal of Methyl Blue Dye Pollutant from Contaminated Water. *RSC Adv.* **2018**, *8*, 8528–8536. [CrossRef]
10. Masudi, A.; Harimisa, G.E.; Ghafar, N.A.; Jusoh, N.W.C. Magnetite-Based Catalysts for Wastewater Treatment. *Environ. Sci. Pollut. Res.* **2020**, *27*, 4664–4682. [CrossRef]
11. Wadhawan, S.; Jain, A.; Nayyar, J.; Mehta, S.K. Role of Nanomaterials as Adsorbents in Heavy Metal Ion Removal from Waste Water: A Review. *J. Water Process Eng.* **2020**, *33*, 101038. [CrossRef]
12. Niculescu, A.-G.; Chircov, C.; Grumezescu, A.M. Magnetite Nanoparticles: Synthesis Methods—A Comparative Review. *Methods* **2022**, *199*, 16–27. [CrossRef] [PubMed]
13. Cabrera, L.; Gutiérrez, S.; Herrasti, P.; Reyman, D. Sonoelectrochemical Synthesis of Magnetite. *Phys. Procedia* **2010**, *3*, 89–94. [CrossRef]
14. Zore, U.K.; Yedire, S.G.; Pandi, N.; Manickam, S.; Sonawane, S.H. A Review on Recent Advances in Hydrogen Energy, Fuel Cell, Biofuel and Fuel Refining via Ultrasound Process Intensification. *Ultrason. Sonochem.* **2021**, *73*, 105536. [CrossRef] [PubMed]
15. Sivasankar, T.; Paunikar, A.W.; Moholkar, V.S. Mechanistic Approach to Enhancement of the Yield of a Sonochemical Reaction. *AIChE J.* **2007**, *53*, 1132–1143. [CrossRef]
16. Cheng, H.; Shapter, J.G.; Li, Y.; Gao, G. Recent Progress of Advanced Anode Materials of Lithium-Ion Batteries. *J. Energy Chem.* **2021**, *57*, 451–468. [CrossRef]
17. Gao, T.; Xu, C.; Li, R.; Zhang, R.; Wang, B.; Jiang, X.; Hu, M.; Bando, Y.; Kong, D.; Dai, P.; et al. Biomass-Derived Carbon Paper to Sandwich Magnetite Anode for Long-Life Li-Ion Battery. *ACS Nano* **2019**, *13*, 11901–11911. [CrossRef]
18. Chen, Q.; Wei, W.; Tang, J.; Lin, J.; Li, S.; Zhu, M. Dopamine-Assisted Preparation of Fe_3O_4@MnO_2 Yolk@shell Microspheres for Improved Pseudocapacitive Performance. *Electrochim. Acta* **2019**, *317*, 628–637. [CrossRef]
19. Minakshi, M.; Mitchell, D.; Prince, K. Incorporation of TiB_2 Additive into MnO_2 Cathode and Its Influence on Rechargeability in an Aqueous Battery System. *Solid State Ionics* **2008**, *179*, 355–361. [CrossRef]
20. Biswal, A.; Panda, P.K.; Acharya, A.N.; Mohapatra, S.; Swain, N.; Tripathy, B.C.; Jiang, Z.-T.; Minakshi Sundaram, M. Role of Additives in Electrochemical Deposition of Ternary Metal Oxide Microspheres for Supercapacitor Applications. *ACS Omega* **2020**, *5*, 3405–3417. [CrossRef]

21. Minakshi, M.; Singh, P.; Mitchell, D.R.G.; Issa, T.B.; Prince, K. A Study of Lithium Insertion into MnO_2 Containing TiS_2 Additive a Battery Material in Aqueous LiOH Solution. *Electrochim. Acta* **2007**, *52*, 7007–7013. [CrossRef]
22. Minakshi, M.; Pandey, A.; Blackford, M.; Ionescu, M. Effect of TiS_2 Additive on $LiMnPO_4$ Cathode in Aqueous Solutions. *Energy Fuels* **2010**, *24*, 6193–6197. [CrossRef]
23. Manickam, M.; Takata, M. Electrochemical and X-Ray Photoelectron Spectroscopy Studies of Carbon Black as an Additive in Li Batteries. *J. Power Sources* **2002**, *112*, 116–120. [CrossRef]
24. Minakshi, M.; Singh, P.; Mitchell, D.R. Manganese Dioxide Cathode in the Presence of TiS_2 as Additive on an Aqueous Lithium Secondary Cell. *J. Electrochem. Soc.* **2007**, *154*, A109. [CrossRef]
25. Kalidass, J.; Sivasankar, T. Facile One-Pot Rapid Sonoelectrochemical Synthesis of Mesoporous Magnetite Nanospheres: A Chimie Douce Approach. *Mater. Chem. Phys.* **2023**, *301*, 127620. [CrossRef]
26. Kalidass, J.; Sivasankar, T. Mesoporous Core/Shell $MnFe_2O_4$ Nanocomposite Derived from Facile Sonoelectrochemical Process: An Eco-Friendly Method for Rapid Synthesis and Versatile Industrial Applications. *J. Taiwan Inst. Chem. Eng.* **2023**, *144*, 104766. [CrossRef]
27. Dong, X.; Wang, J.; Miao, J.; Ren, B.; Wang, X.; Zhang, L.; Liu, Z.; Xu, Y. Fe_3O_4/MnO_2 Co-Doping Phenolic Resin Porous Carbon for High Performance Supercapacitors. *J. Taiwan Inst. Chem. Eng.* **2022**, *135*, 104385. [CrossRef]
28. Dubey, M.; Challagulla, N.V.; Kumar, R. Synergistic Engineering for Adsorption Assisted Photodegradation of 2,4 Dichlorophenol Using Easily Recoverable α-MnO_2/Fe_3O_4 Nanocomposite. *Appl. Surf. Sci. Adv.* **2022**, *11*, 100300. [CrossRef]
29. Zhang, H.; He, Y.; Lai, L.; Yao, G.; Lai, B. Catalytic Ozonation of Bisphenol A in Aqueous Solution by Fe_3O_4-MnO_2 Magnetic Composites: Performance, Transformation Pathways and Mechanism. *Sep. Purif. Technol.* **2020**, *245*, 116449. [CrossRef]
30. Dong, Z.; Zhang, Q.; Chen, B.-Y.; Hong, J. Oxidation of Bisphenol A by Persulfate via Fe_3O_4-α- MnO_2 Nanoflower-like Catalyst: Mechanism and Efficiency. *Chem. Eng. J.* **2019**, *357*, 337–347. [CrossRef]
31. Xiong, Y.; Chen, S.; Ye, F.; Su, L.; Zhang, C.; Shen, S.; Zhao, S. Preparation of Magnetic Core–Shell Nanoflower Fe_3O_4@MnO_2 as Reusable Oxidase Mimetics for Colorimetric Detection of Phenol. *Anal. Methods* **2015**, *7*, 1300–1306. [CrossRef]
32. Zhang, C.; Jin, C.; Teng, G.; Gu, Y.; Ma, W. Controllable Synthesis of Hollow $MnFe_2O_4$ by Self-Etching and Its Application in High-Performance Anode for Lithium-Ion Batteries. *Chem. Eng. J.* **2019**, *365*, 121–131. [CrossRef]
33. Wang, N.; Ma, X.; Wang, Y.; Yang, J.; Qian, Y. Porous $MnFe_2O_4$ Microrods as Advanced Anodes for Li-Ion Batteries with Long Cycle Lifespan. *J. Mater. Chem. A* **2015**, *3*, 9550–9555. [CrossRef]
34. Yang, Z.; Huang, Y.; Ji, D.; Xiong, G.; Luo, H.; Wan, Y. Hydrazine Hydrate-Induced Hydrothermal Synthesis of $MnFe_2O_4$ Nanoparticles Dispersed on Graphene as High-Performance Anode Material for Lithium Ion Batteries. *Ceram. Int.* **2017**, *43*, 10905–10912. [CrossRef]
35. Tang, H.; Gao, P.; Xing, A.; Tian, S.; Bao, Z. One-Pot Low-Temperature Synthesis of a $MnFe_2O_4$–Graphene Composite for Lithium Ion Battery Applications. *RSC Adv.* **2014**, *4*, 28421–28425. [CrossRef]
36. Wang, F.; Li, T.; Fang, Y.; Wang, Z.; Zhu, J. Heterogeneous Structured Mn_2O_3/Fe_2O_3 Composite as Anode Material for High Performance Lithium Ion Batteries. *J. Alloys Compd.* **2021**, *857*, 157531. [CrossRef]
37. Wang, D.; Wang, Y.; Li, Q.; Guo, W.; Zhang, F.; Niu, S. Urchin-like α-Fe_2O_3/MnO_2 Hierarchical Hollow Composite Microspheres as Lithium-Ion Battery Anodes. *J. Power Sources* **2018**, *393*, 186–192. [CrossRef]
38. Fu, Y.; Wang, X.; Wang, H.; Zhang, Y.; Yang, X.; Shu, H. An Fe_3O_4@(C–MnO_2) Core–Double-Shell Composite as a High-Performance Anode Material for Lithium Ion Batteries. *RSC Adv.* **2015**, *5*, 14531–14539. [CrossRef]
39. Guan, B.; Sun, W.; Wang, Y. Carbon-Coated MnMoO4 Nanorod for High-Performance Lithium-Ion Batteries. *Electrochim. Acta* **2016**, *190*, 354–359. [CrossRef]
40. Minakshi, M.; Barmi, M.; Mitchell, D.R.; Barlow, A.J.; Fichtner, M. Effect of Oxidizer in the Synthesis of NiO Anchored Nanostructure Nickel Molybdate for Sodium-Ion Battery. *Mater. Today Energy* **2018**, *10*, 1–14. [CrossRef]
41. Chu, Y.; Shi, X.; Wang, Y.; Fang, Z.; Deng, Y.; Liu, Z.; Dong, Q.; Hao, Z. High Temperature Solid-State Synthesis of Dopant-Free $Fe_2Mo_3O_8$ for Lithium-Ion Batteries. *Inorg. Chem. Commun.* **2019**, *107*, 107477. [CrossRef]
42. Xue, R.; Hong, W.; Pan, Z.; Jin, W.; Zhao, H.; Song, Y.; Zhou, J.; Liu, Y. Enhanced Electrochemical Performance of $ZnMoO_4$/Reduced Graphene Oxide Composites as Anode Materials for Lithium-Ion Batteries. *Electrochim. Acta* **2016**, *222*, 838–844. [CrossRef]